Three-Dimensional and Time-Ordered Surface-Enhanced Raman Scattering Hotspot Matrix

Honglin Liu,[†] Zhilin Yang,[‡] Lingyan Meng,[‡] Yudie Sun,[†] Jie Wang,[§] Liangbao Yang,*,[†] Jinhuai Liu,*,[†] and Zhongqun Tian[‡]

[†]Institute of Intelligent Machines, Chinese Academy of Sciences, Hefei 230031, China

[‡]State Key Laboratory of Physical Chemistry of Solid Surfaces and College of Chemistry and Chemical Engineering, Xiamen University, Xiamen 361005, China

[§]Shanghai Synchrotron Radiation Facility, Shanghai Institute of Applied Physics, Chinese Academy of Sciences, Shanghai 201204, China

Ⓢ Supporting Information

ABSTRACT: The "fixed" or "flexible" design of plasmonic hotspots is a frontier area of research in the field of surface-enhanced Raman scattering (SERS). Most reported SERS hotspots have been shown to exist in zero-dimensional point-like, one-dimensional linear, or two-dimensional planar geometries. Here, we demonstrate a novel three-dimensional (3D) hotspot matrix that can hold hotspots between every two adjacent particles in 3D space, simply achieved by evaporating a droplet of citrate-Ag sols on a fluorosilylated silicon

wafer. In situ synchrotron-radiation small-angle X-ray scattering (SR-SAXS), combined with dark-field microscopy and in situ micro-UV, was employed to explore the evolution of the 3D geometry and plasmonic properties of Ag nanoparticles in a single droplet. In such a droplet, there is a distinct 3D geometry with minimal polydispersity of particle size and maximal uniformity of interparticle distance, significantly different from the dry state. According to theoretical simulations, the liquid adhesive force promotes a closely packed assembly of particles, and the interparticle distance is not fixed but can be balanced in a small range by the interplay of the van der Waals attraction and electrostatic repulsion experienced by a particle. The "trapping well" for immobilizing particles in 3D space can result in a large number of hotspots in a 3D geometry. Both theoretical and experimental results demonstrate that the 3D hotspots are predictable and time-ordered in the absence of any sample manipulation. Use of the matrix not only produces giant Raman enhancement at least 2 orders of magnitude larger than that of dried substrates, but also provides the structural basis for trapping molecules. Even a single molecule of resonant dye can generate a large SERS signal. With a portable Raman spectrometer, the detection capability is also greatly improved for various analytes with different natures, including pesticides and drugs. This 3D hotspot matrix overcomes the long-standing limitations of SERS for the ultrasensitive characterization of various substrates and analytes and promises to transform SERS into a practical analytical technique.
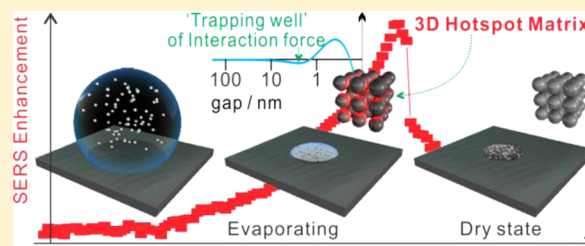
■ INTRODUCTION

The discovery of the "hotspot" for ultrahigh surface-enhanced Raman scattering (SERS) enhancement,[1] with the ultimate goal of reliably identifying single molecules,[2] has led to the in-depth development of methods for tuning the plasmonic properties of metallic nanostructures.[3,4] The construction of "fixed" hotspots on solid substrates by preparing oriented assemblies of functional nanoparticles, such as SHINERS,[5] core–shell monomers,[6] dimers,[7,8] trimers,[9] chains[10] or arrays,[11] is a frontier area of research in the SERS community. In addition, "flexible" designs utilizing electronic,[12] ferroelectric,[13] thermal,[14] mechanical strain,[15] or capillary[16] effects have allowed for the tunability of plasmonic hotspots. However, the electromagnetic enhancement is highly distance dependent.[17] To maximize the electric field experienced by a molecule, one of the most critical issues has been the subnanometer control of the gap size.[18] Although molecular-sized gaps can be produced

by particle aggregates,[9] break junctions,[19] or lithography,[20] there are problems of structural reproducibility, low yield, and high cost. Furthermore, steric hindrance may prevent the entrance of a molecule into a gap even if the gaps are precisely prefabricated. In particular, the self-assembly of particles on solid substrates can produce a high yield of sub-10-nm gaps when the metal surface is modified with different capping agents.[11,21] Recently, self-assembled particle arrays on liquid/liquid interfaces have been used for liquid-state SERS.[22,23] These closely packed nanostructures produce multiple hotspots in a uniform fashion over a large area, but the density of these hotspots is ultimately limited by the two-dimensional plane. In brief, these types of hotspots distribute in zero-, one-, or two-

dimensional geometries and exist in a single, isolated, and unordered or uncontrollable manner. Does a 3D hotspot matrix exist that can host hotspots between every two adjacent particles in 3D space? In fact, robust control over the orientation and position of nanoparticles in 3D geometry remains a formidable challenge because of thermal fluctuations and diffusion.[23] Quite recently, an amphiphilic diblock copolymer has been successfully used to functionalize gold nanoparticles for assembling particles into stable 3D clusters, and it was found that the optical properties of the clusters depended on particle number and cluster geometry.[24] The simplest and most random symmetrical system with 3D geometry is a droplet of noble-metal nanoparticle sols.

In this study, a novel 3D hotspot matrix was readily achieved by evaporating a droplet of citrate-Ag sols on a fluorosilylated silicon wafer. In the 3D space of this droplet, the interparticle gaps shrink significantly as water evaporates until the particles are uniformly deposited on the surface. This evaporation process was analyzed using in situ synchrotron-radiation small-angle X-ray scattering (SR-SAXS) to directly monitor the aggregation process and spatial distribution. Using this method, the shape, size, interparticle distance, and particle density may be determined in situ by probing the original microliter colloid without further sample manipulation.[25] By applying this analytical method in conjunction with such techniques as SEM, AFM, dark-field microscopy, and in situ micro-UV, this article first explores the evolution of Ag nanoparticles during the evaporation process. On the basis of these comprehensive data and theoretical simulations of interparticle interactions, a mechanistic scheme for the formation of the 3D hotspot matrix is proposed. During this process, particle−particle interactions via van der Waals attraction and electrostatic repulsion can create a "trapping well" to immobilize particles in 3D space and result in a large number of hot spots with 3D geometry. The number of hotspots and the 3D electric-field distributions were also calculated using the Monte Carlo and finite element methods, respectively, and the validity of these calculations was ultimately demonstrated by the excellent SERS performance of the prepared matrix.

EXPERIMENTAL SECTION

In situ SR-SAXS was used to directly monitor nanoparticle distributions in 3D space. The μSpot beamline BL16B1 at SSRF (Shanghai, China) was used to measure time-resolved SR-SAXS data, which were processed and fitted using the Fit2D and Irena software packages.[26] An inverted microscope (eclipse Ti−U, Nikon, Japan) equipped with a dark-field condenser (0.8 < NA < 0.95) and a 40× objective lens (NA = 0.8) was used by Prof. Long's group (ECUST, Shanghai) for the real-time monitoring of the morphological alterations of particle aggregates in Ag sols.[27] A novel experimental setup using only one optics-integrating sphere was designed to measure the plasmonic properties of a single microliter droplet; termed in situ micro-UV (NOVA, ideaoptics instruments, China), this technique was performed by Shanghai NTI Co., Ltd. (Shanghai, China). A LabRam HR800 confocal micro-Raman system (JY Horiba) was used to collect Raman spectra under the same conditions: the excitation line was 532 nm from a Nd:YAG laser focused by a LWD 50×/0.5 NA objective lens; the laser power was 0.2 mW, and the laser spot had a diameter (Φ) of ∼1.29 μm; the grating was 600 g/mm; the exposure time for each spectrum was 1 s; and the increment time in time-course SERS mapping was 2 s. A portable Raman spectrometer (Inspetor, DeltaNu, USA) with an excitation laser of 785 nm was used. In sample preparation, for example, 1 μL of 50 pmol/L R6G aqueous solution was added to 1 μL of the concentrated Ag sols (≈10^{10} particles/μL, Supporting Information Figure S1) to prepare a 2-μL

Raman sample, providing 50 amol molecules for detection. To avoid errors caused by accidentally introduced molecules, each SERS experiment was controlled by first measuring an analyte-free sample as a reference. All chemicals were of analytical grade (≥99.8%), and the experimental details are provided in the Supporting Information.

RESULTS AND DISCUSSION

Here, we present a 3D hotspot matrix and the synergy between its ultrahigh SERS enhancement and its molecule-trapping capability. Ideally, a spherical droplet of particle sols in 3D space will become smaller as water evaporates from the droplet surface, the particles are pulled toward each other, and the analyte molecules are wicked up and become trapped between the closely packed particles. Figure 1a provides an approximate illustration of such a system.

A 1-μL droplet of Ag sols with a concentration of ∼10^{10} particles/μL was placed on a silicon wafer. The wafer surface was hydrophobically treated with fluorosilane and had a contact angle of approximately 107° (Supporting Information Figure S2a). Complete drying of this droplet at 25 °C required approximately 10 min. After the first 9 min, the droplet height
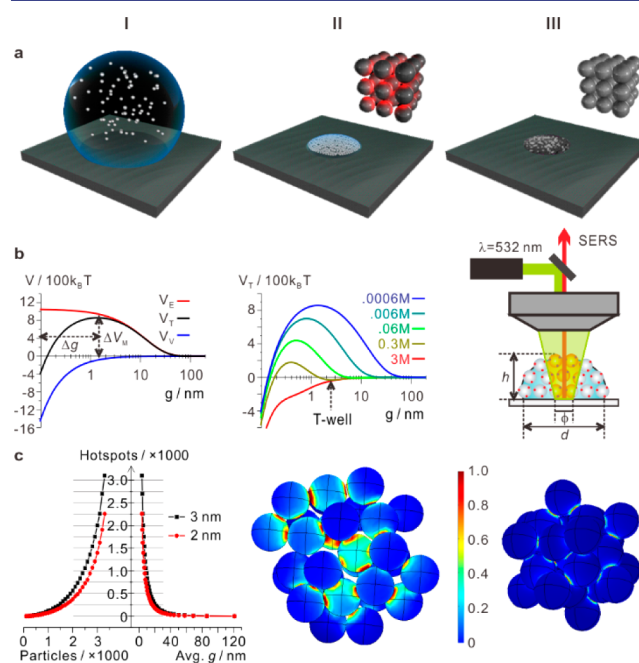

Figure 1. 3D hotspot matrix of noble-metal sols generated in the water evaporation process. (a) Sketches representing (I) a droplet of Ag sols on a hydrophobic surface, (II) the adhesive-force-constructed closely packed particles in 3D space formed in the water-evaporation process, and (III) the aggregation and deposition of particles on the dried substrate, which quenches the 3D hotspot matrix. (b) (I) Interaction energy between citrate-Ag particles as a function of g at I = 0.6 mM, (II) total interaction energy as a function of g at different I, and (III) schematic of SERS measurements on a droplet. The laser spot is focused on the substrate surface and has a diameter, φ, of approximately 1 μm. (c) Theoretical simulations. (I) The calculated number of hotspots as a function of the number of particles (left) and the average g (right) within an ideal spherical droplet of 1 μm in diameter, where a hotspot is defined by g ≤ 3 nm or g ≤ 2 nm, respectively, (II) distribution of electric-field intensity |E(r)|² for 35 Ag particles of 50 nm in diameter dispersed randomly in a water drop of 1 μm in diameter, and (III) that for the randomly placed Ag aggregates. The color bar indicates normalized values for convenience of comparison.

(*h*) decreased to ∼50 *μ*m (Supporting Information Figure S2b). When the remaining droplet was discarded, no particles were adsorbed on this surface (Supporting Information Figure S2c). Finally, the droplet dried in an area of approximately 0.8 mm in diameter (*d*) (Supporting Information Figure S3a). Assuming uniform distribution of all particles, a particle density of approximately 2×10^4 particles/μm^2 was obtained. If each particle was 50 nm in diameter (*R*), then there were approximately 50 layers of particles ($h \approx 2.5 \ \mu$m). This estimation was evidenced by AFM observations and cross-sectional SEM images (Supporting Information Figure S4). Moreover, the assembled multilayer had a uniform height in large range (Supporting Information Figure S4b), the "coffee ring effect"[28] was greatly weakened (Supporting Information Figure S3), and the liquid adhesive force promoted the closely packed assembly of the particles (Supporting Information Figure S5), unlike the strong electrostatic effect of the hydrophilic surface. Accordingly, an approximate model for the later stage of the water-evaporation process was established (Supporting Information Figure S6d). As the content of the liquid phase decreased in the nonequilibrium evaporation process, the greatest effect of the liquid bridge between two Ag particles was cohesion between particles (Supporting Information Figure S7). The capillary force becomes dominant when the relevant length scales are much smaller than the capillary length of water (∼3.9 mm, Supporting Information eq S4), and the calculated adhesive force between Ag particles is far greater than their gravities (Supporting Information eq S7). Hence, construction of a 3D architecture of liquid-bridged nanoparticles that can maintain specific gap sizes between every two adjacent particles is quite possible.

To quantitatively understand our hypothesis, we performed theoretical simulations for an ideal spherical droplet of Ag sols with a diameter of 1 *μ*m. The number of hotspots among the Ag particles in 3D space was calculated using the Monte Carlo method, which relies on repeated random sampling to obtain numerical results (Supporting Information Section S3.5). A valid hotspot was defined as either $g \leq 3$ nm or $g \leq 2$ nm. The number of hotspots is plotted in Figure 1c-I; a significant exponential increase is observed with decreasing average *g* (corresponding to an increasing number of particles). In particular, if there are 3300 particles of 50 nm in diameter in a droplet of 1 *μ*m in diameter and $g \leq 3$ nm defines a valid hotspot, then the calculated number of hot spots is 3100. In this case, the total volume of all particles is only 40% of the droplet volume; therefore, the number of 3D hotspots should further increase as the particle density increases. Ideally, the total number of hotspots in a well-assembled 2D array is three times the number of particles. In a deposition area of 1 *μ*m in diameter, there are approximately 314 nanospheres of 50 nm in diameter, i.e., the maximum number of hotspots in a 2D array is approximately 950, much less than one-third the number of 3D hotspots. Therefore, the density of these hotspots is ultimately limited by the 2D plane, and a 3D hotspot matrix can greatly increase the number of hotspots.

The electric-field distributions of Ag particles distributed randomly in 3D space was calculated using the finite element method (Supporting Information Section S3.6). Figure 1c-II and 1c-III present the calculated results for 35 Ag particles with average $g = 2$ nm and average $g = 0$ nm, respectively, representing two states in the dynamic process of solvent evaporation. Note that these two near-field images are normalized to obtain the relative variation of the electric-field

enhancement. For average $g = 2$ nm, many hotspots and a giant electric-field enhancement were obtained. Furthermore, decreasing the average *g* value to zero causes the particles to aggregate tightly; surprisingly, the electric-field enhancement sharply decreases even though many more hotpots are to be formed. The maximum electric-field enhancement decreases by 30%. Three explanations can be applied to interpret this calculated result. First, when *g* is smaller than 1 nm, quantum tunneling arises and dramatically reduces the electromagnetic enhancement ability. Second, as the particles touch each other, charge-exchange phenomena occur, leading to a decrease in the electric-field enhancement. Finally, solid contacts among particles cause the entire aggregate to behave as an equipotential body and thus give rise to an electrostatic shielding phenomenon that further decreases the electric-field enhancement. Interestingly and importantly, these calculations are consistent with the experiments discussed below.

There are free citrate and nitrate anions and sodium cations in the Ag sol system prepared via the trisodium-citrate reduction method. The ionic strength increases as the droplet volume decreases during the nonequilibrium evaporation process. To clearly observe the effect of ionic strength, the as-synthesized Ag sols were 10-fold diluted with citrate solutions of different concentrations. The effect of ionic strength (trisodium citrate) on the evolution of the aggregating structure during the drying of the Ag sols was clearly observed via SEM and UV−vis spectroscopy (Figure 2). Colloids with
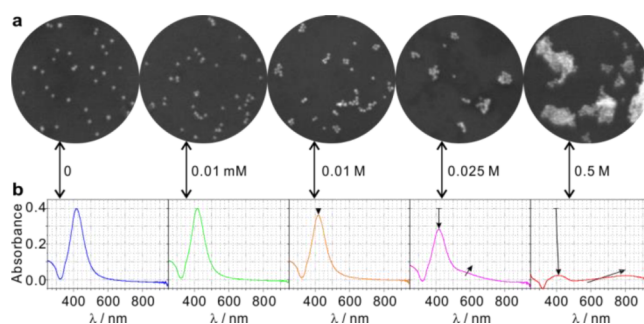

Figure 2. Effect of citrate concentration on the preaggregation of Ag sols. (a) The addition of an increasing quantity of citrate increases the number of aggregated particles in solution, as observed via SEM. Each sample of Ag sols was 10-fold diluted with citrate solution of a given concentration indicated by the labels in the figure. (b) The corresponding surface-plasmon resonance (SPR) properties observed via UV−vis spectroscopy.

low concentrations of citrate have high dispersion and an SPR peak located at approximately 410 nm. When the salt concentration is increased in the sol, the nanoparticles aggregate via a diffusion-limited mechanism, leading to a polydisperse mixture of essentially unaggregated nanoparticles and porous aggregates, two distinct "particle" populations. This alteration is reflected in the plasmonic properties by the weakening of the SPR peak at approximately 410 nm and the emergence of a new SPR shoulder peak at approximately 500−800 nm (Figure 2b). During subsequent drying, the evolution of the aggregating structure is controlled by aggregate−aggregate, aggregate−nanoparticle, and nanoparticle−nanoparticle aggregation processes.

We anticipated that the evolution of porosity in such a system should be strongly influenced by the concentrations of both salt and nanoparticles. When the 100-fold concentrated

Ag sols dried on the surface of a fluorosilylated silicon wafer, a closely packed assembly formed a multilayer film of particles with a height of approximately 2 μm (Supporting Information Figure S4), which is consistent with the theoretical calculations presented above. An important unifying concept underlying these observations is the central role played by preaggregation in controlling the structural evolution during evaporation, and some aggregation would be expected to occur as the concentration of citrate is increased. Preaggregation plays an important role in controlling both the porosity and morphology of the assembling structures.[29]

We must now investigate under which conditions the sol particles will construct a 3D hotspot matrix instead of aggregating in bulk. In the case of aggregation, classical DLVO theory[30] describes the interplay of the van der Waals attractive (V_V) and electrical double-layer repulsive (V_E) potentials experienced by a particle when approaching another particle for a given set of conditions related to ionic strength and surface potentials. The total interaction potential between two citrate-AgNPs (V_T) can be expressed as the sum of V_V and V_E:

$$V_T = V_V + V_E \tag{1}$$

The van der Waals attraction potential, V_V, between two identical spherical Ag particles (each with radius of r) can be calculated as[31,32]

$$V_V = f(g) = -\frac{A_H r}{12g(1 + 14g/\lambda)} \tag{2}$$

or as[30]

$$V_V = f(g)$$
$$= -\frac{A_H}{6}\left[\frac{2r^2}{(2r+g)^2 - 4r^2} + \frac{2r^2}{(2r+g)^2} + \ln\frac{(2r+g)^2 - 4r^2}{(2r+g)^2} \right] \tag{2'}$$

The Hamaker constant A_H plays an important role in the description of the attraction energy between particles, and a typical A_H is 28.2×10^{-20} J for unretarded interaction between AgNPs in water.[31] Depending on the particle size and the double-layer thickness, the electrostatic repulsion potential, V_E, between two identical colloidal Ag particles of radius r can be expressed in the following form:[31,33]

$$V_E = f(g) = 32\pi\varepsilon_0\varepsilon_r r\left(\frac{k_B T}{ze}\right)^2 \psi_0^2 \exp(-\kappa g) \tag{3}$$

The potential ψ_0 at the particle surface can be estimated from the ζ potential measurement, which is approximately -37 mV for citrate-AgNPs.[34] The inverse Debye length at 298 K can be calculated from

$$\kappa = \left[\frac{1000e^2 N_A (2I)}{\varepsilon_0 \varepsilon_r k_B T} \right]^{1/2} = 3.257 \times 10^9 \sqrt{I}$$

$$\Leftrightarrow \kappa^{-1}\,(\text{nm}) = \frac{0.307}{\sqrt{I\,(\text{M})}} \tag{4}$$

Figure 1b-I shows the calculated g-dependent V_V, V_E, and V_T to describe the initial state of a droplet of Ag sols, and the maximum energy barrier (ΔV_M) is hundreds of times larger

than the particle kinetic energy of Brownian motion ($\sim 0.5 k_B T$).[35,36] Nevertheless, the ionic strength I strongly affects the height of this barrier. I, which is inversely proportional to the droplet volume, is increased by a factor of approximately 766 at $g = 2$ nm (Supporting Information eq S2). At higher ionic strengths, the thickness of the double layer decreases (eq 4); thus, the effects of repulsion are not felt until the two particles are relatively near each other, where attractive forces become significant. At $g < \Delta g$, a repulsive V_E gives way to an attractive V_V in a region called the primary energy minimum (Figure 1b-I).

Interestingly, at $I = 0.3$ M for the conditions assumed (Figure 1b-II), another region of attractive V_V dominance appears, centered at a g of approximately 2–3 nm. This second region is called the secondary energy minimum and is evident in Figure 1b-II for an ionic strength of 0.3 M; it acts as a trapping well (T-well) to immobilize particles. Theoretically, this T-well is important to the construction of the 3D hotspot matrix when the T-well depth is such that particles do not possess sufficient energy to escape. In fact, the thermal energy of Brownian particles is generally less than a few $k_B T$,[31,32] and the V_T associated with a T-well is approximately $-30 k_B T$ at $g = 2$–3 nm and $I = 0.3$ M, which could guarantee the particle stability of this system for a period of at least 1 h (see the estimation of colloidal stability in the late-stage evaporation process in Supporting Information Section 3.4). Thus, the T-well would be expected to effectively trap and immobilize such particles and generate a 3D hotspot matrix in space.

Does the T-well truly exist? Dark-field optical microscopy was employed to trace the morphological alterations of a specific aggregate in real time during the evaporation process (Figure 3). Moreover, four additional aggregates were
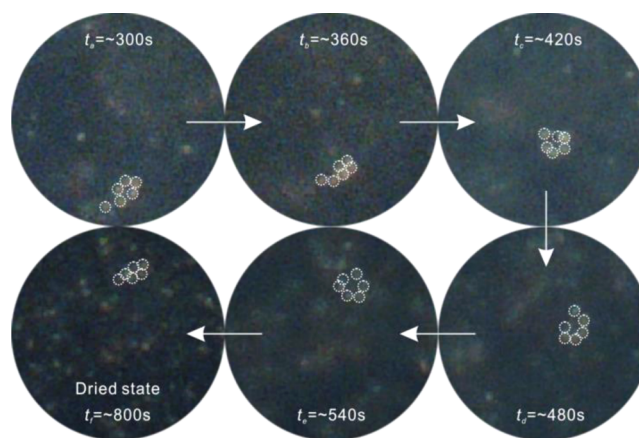

Figure 3. Dark-field optical microscopy for real-time tracing of the morphological alterations of a specific aggregate in the evaporation process of a 1-μL sample. This sample of Ag sols was 10-fold diluted with 0.01 mM citrate solution to avoid overly strong light scattering.

simultaneously traced (Supporting Information Figure S8). The microscope focus was manually adjusted in real time to ensure that the object of interest was distinctly in view until the evaporation was complete. In the later stage of evaporation, some relatively large aggregations of Ag particles began to appear ($t = \sim 300$ s). Interestingly, the morphology of this aggregation was not fixed and changed noticeably over time, and this object gradually moved from the bottom of the dark field to the top. However, at $t = \sim 800$ s, the droplet was dried completely, as evidenced by the clear observation of all objects

in the dark field. Significantly, this object of interest tightened and aggregated completely, and the simultaneous tracing of four additional aggregates produced similar results (Supporting Information Figure S8). In reality, an Ag particle is not perfectly spherical, and the capping of citrate groups on the Ag surface is not uniform. Hence, real particles are more susceptible to their chemical environments. Nevertheless, one point remains certain: the continuous increase of ionic strength and particle density in the evaporation process can create a critical state that can balance the interplay of V_V and V_E experienced by a particle and control the interparticle distance within a small range, and this state is clearly different from the dried state.

To monitor the evolution of the plasmonic properties of a single droplet during its evaporation, one optics-integrating sphere was used in conjunction with a fiber-optic spectrometer to collect the UV−vis spectrum of a single droplet of 1-μL Ag sols (Figure 4a). The time-resolved optical behavior of the
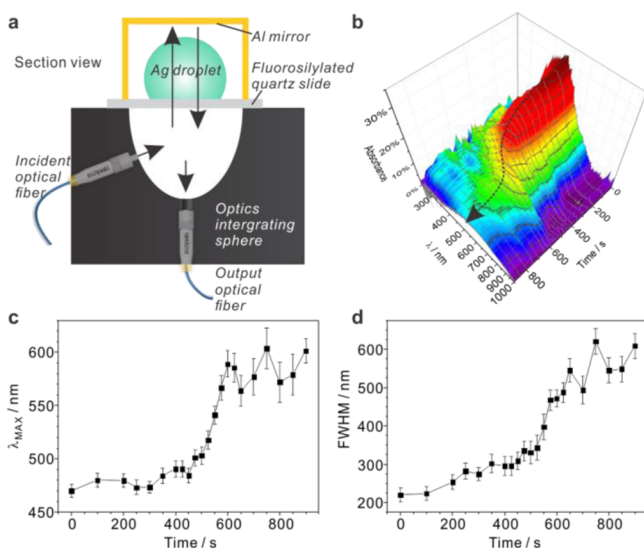

Figure 4. (a) Schematic cross-sectional view of the in situ micro-UV setup used to measure the plasmonic properties of a single droplet of a 1-μL Ag sample throughout its evaporation process. (b) Time-dependent UV−vis absorbance spectrum. (c) SPR peak position (λ_{MAX}) and (d) fwhm plotted as functions of time, as derived from UV−vis data.

colloids could be precisely followed (Figure 4b). The peak position and fwhm should be indicative of particle size or aggregation extent, although the interpretation of UV−vis data and the particle-aggregation mechanism remain controversial. Figure 4c shows the evolution of an absorbance maximum in the 480 to 600 nm range, which is typically ascribed to the plasmon resonance of Ag nanoparticles, nanoparticle−nanoparticle, aggregate−nanoparticle, or aggregate−aggregate aggregation. During the experiment, the apparent peak maximum (λ_{MAX}) shifted rapidly from approximately 500 nm to approximately 580 nm in the final colloid, and the peak fwhm gradually broadened from 225 to 600 nm. The intensity at each respective maximum peak position can also be identified in Figure 4b. The changes in intensity, peak position, and fwhm all reflect the typically observed time dependence, with a slow initial alteration followed by a more rapid one.

To examine the 3D geometry of Ag particles in a droplet in situ during its evaporation process, in situ SR-SAXS was employed to directly monitor a single droplet of concentrated

Ag sols on a fluorosilylated quartz slide without further sample manipulation. The developed SR-SAXS setup is schematically depicted in Figure 5a,b. Initially, a quartz slide was placed on the horizontal sample stage. The X-ray beam had a beam spot of approximately 200 μm × 400 μm, which was swept past the surface of the sample stage, and the tilt angle of the sample stage was zero degrees. Under these conditions, the background scattering of the quartz slide could be neglected (Supporting Information Figure S9), and structural information near the slide surface could be obtained. In the later stage of evaporation, the sample stage was slightly tilted by 0.2° to increase the signal strength and to further corroborate the final state of the sample. A single droplet of 15-μL Ag sols was placed in the light path to ensure in situ SR-SAXS observation throughout the evaporation process, which had a duration of approximately 1 h. The time resolution of the SR-SAXS was approximately 8 s, which corresponds to the data-acquisition time plus the hardware and software response times. Figure 5c presents four typical 2D SR-SAXS patterns at four different times, and the 2D patterns were processed and converted into diagrams of scattered intensities (I) vs scattering vector (q) by integration over an azimuthal range of −165 to 165°. The scattering vector q is defined in terms of the scattering angle θ and the radiation wavelength λ as follows: $q = 4\pi \, (\sin\theta)/\lambda$.[25]

The scattering signal originates from the contrast between the Ag nanoparticles and the solvent or air. The definition of the interparticle distance in the 3D geometry of a SAXS sample is the statistical average distance between particles (or a). For a dense system, a scattering maximum will emerge in the scattering curves and will become increasingly sharp with an increase in the uniformity of the particle size and interparticle distance. Figure 5c2 displays an obvious peak at $q = 0.138$, indicating that the assembly of Ag particles in the evaporation process exhibits a long-range-ordered structure after approximately 47 min. Figure 5d presents the total SR-SAXS scattering curves obtained throughout the entire experiment in log−log coordinates. The dotted arrow clearly indicates the emergence and rightward shift of the signal peak. This phenomenon reflects the scattering interference between particles. When the scattering maximum is high and narrow, the interparticle distance can be calculated according to the Bragg formula: $2a \sin \theta = \lambda$.

By contrast, both an increase in the polydispersity of the particle size and a decrease in the uniformity of the interparticle distance can cause the lowering and broadening of the scattering maximum; sometimes, the scattering maximum becomes a shoulder peak, corresponding to the superposition of interparticle distances of different magnitudes in the scattering curve. The latter phenomenon is more common in both the initial and final stages of the evaporation process. In these cases, the Lorentz correction method was used to accurately determine the position of the scattering maximum; the intensity I of the SAXS curves was transformed into $q^4 \cdot I$ plotted as a function of q (Figure 5e).[26] Moreover, the fwhm of the transformed scattering maximum should be an additional indicator of particle size and interparticle distance. Higher and narrower peaks indicate more regular particle sizes and interparticle distances.

The characteristic colloid properties deduced from the in situ SR-SAXS data are presented in Figure 5f (peak-intensity variation), 5g (particle density), 5h (peak position and fwhm), and 5i (the particles' mean radius and normalized center-to-center distance). The scattering intensity and peak position
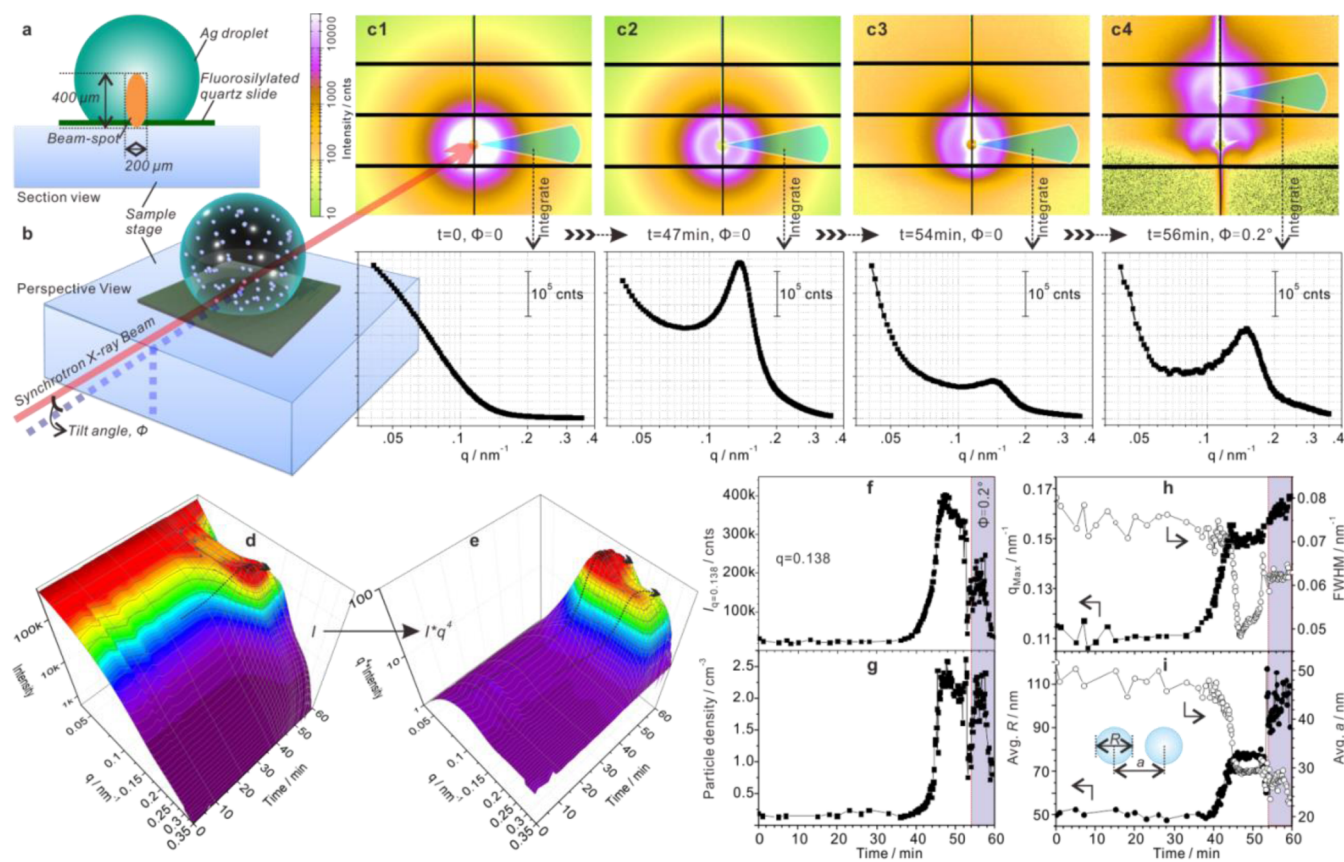
Figure 5. Schematic (a) cross-sectional and (b) perspective views of the experimental setup used for SR-SAXS analysis of a single droplet of a 15-μL Ag sample during the evaporation process, indicating the sample position, the beam-spot size, and the direction of the synchrotron X-ray beam (λ = 1.04 Å). (c) Four typical 2D SR-SAXS patterns and their corresponding SR-SAXS curves obtained by integration over an azimuthal range of −165 to 165° recorded at four different times. The tilt angle of the sample stage is 0° in c1−c3 and 0.2° in c4, and the upper SR-SAXS pattern in c4 originates from light reflection. (d) Time-dependent SR-SAXS curves acquired during the evaporation process, plotted as SR-SAXS intensity (I) vs scattering-vector modulus (q); the dotted arrow indicates the emergence and rightward shift of the I peak. (e) The transformed SR-SAXS curves in (d), plotted as $q^4 \cdot I$ vs q; the two dotted arrows indicate the emergence and rightward shift of the $q^4 \cdot I$ peaks. Time-dependent (f) I values at q = 0.138, (g) particle density, (h) peak position (q_{MAX}, solid squares) and full width at half-maximum (fwhm, hollow squares), and (i) mean sphere diameter (R, solid circles) and normalized center-to-center distance (a, hollow circles), all of which were derived from the SR-SAXS data presented in (d) and (e).

reach their maximum values and the peak fwhm reaches its minimum value after approximately 47 min. Interestingly, the calculated peak density reaches its maximum value at approximately 47 min and then begins to decrease, even though the irradiation volume was greatly increased when the tilt angle of the sample stage was changed to 0.2°. This result might be consistent with the aggregation of Ag nanoparticles into large particles in the dry state; such particle aggregation would greatly weaken the contrast between the Ag nano-particles and the solvent or air and subsequently reduce the volume fraction of scattering. This conclusion is also supported by the calculated particle size (R) and interparticle distance (a) (Figure 5i). One point should be noted that the fitted a values were generally smaller than the real values. For example, at dry state, the smallest values of a should be equal to the particle diameter, but the calculated values of a decreased to ∼20−30 nm. In a dense and time-varying system, some assumptions in fitting model[26] may be not perfect and induce the deviation of fitting results. But the changing trend of a values is completely same to micro-UV results and following SERS experiments. We considered that the fitted a can be used as a visualized indicator to show the 3D organization of nanoparticles.

The experimental evidence derived from SEM, real-time tracing of dark-field microscopy, in situ micro-UV, and in situ

SR-SAXS reveals that a truly distinct 3D geometry of the Ag particles develops during the evaporation process. This type of 3D geometry has minimal polydispersity of particle size and maximal uniformity of interparticle distance, both of which differ significantly from the dry state. In this intermediate 3D geometry, the liquid adhesive force promotes the closely packed assembly of the particles, and the interparticle distance is not fixed but is rather balanced by the interplay of V_V and V_E experienced by a particle, which controls the interparticle distance to remain within a small range. The modified plasmonic properties imply that this 3D geometry can certainly produce a large number of hot spots in 3D space and amplify the SERS enhancement accordingly.

To verify our hypothesis, time-course SERS mapping was performed to monitor the evaporation of a 1-μL sample (Figure 6 and Supporting Information Video SI). This initial sample contained 50 amol of rhodamine 6G (R6G); 500 amol of R6G would have induced saturation of the CCD detector under our conditions. During the first 300 s, no Raman signals were observed, and the peak fitting at ∼610 cm^{-1} resulted in nonsensical peak shapes (the frequency and fwhm indicated by hollow squares in Figure 6c,d). Nevertheless, the fingerprints of R6G gradually appeared after ∼300 s; the fitted peak at approximately 610 cm^{-1} exhibits an intensity of approximately
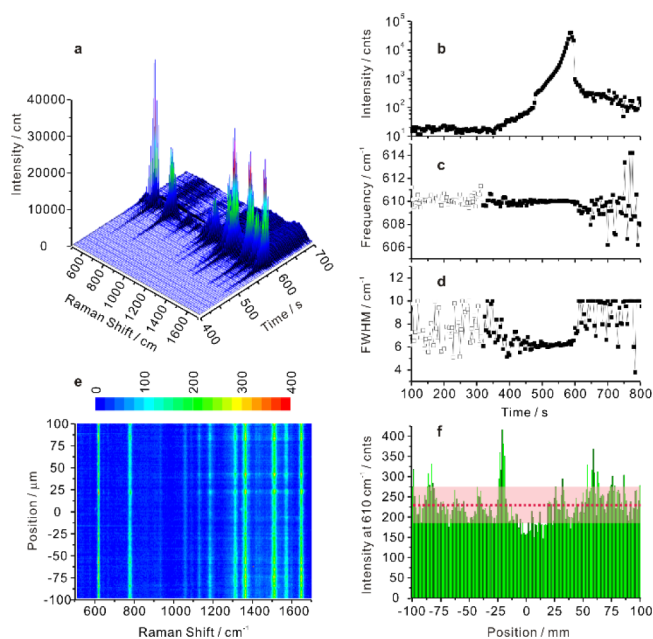
Figure 6. (a) Time-course SERS mapping of a 1-μL sample with 50 amol of R6G (3×10^7 molecules) and $\sim 10^{10}$ Ag particles placed on a hydrophobic-treated silicon wafer. The corresponding time evolution of the (b) intensity, (c) frequency, and (d) full width at half-maximum (fwhm) of the 610 cm^{-1} peak. (e) Line SERS mapping and (f) the corresponding intensities at 610 cm^{-1} for the dried sample in a range of −100 to 100 μm centered on the position used for time-course mapping.

20 cps (Figure 6b) and has large fluctuations in its peak shape. Gradually, these weak signals became stronger and achieved their highest values at ∼580 s; for example, the intensity of the 610 cm^{-1} peak increased to approximately 40 000 cps, approximately 2000 times its initial value. Interestingly, the peak shape also became increasingly stable, and its intensity increased. However, after ∼600 s, the peak intensity rapidly decreased to below approximately 200 cps, and the peak shape again began to fluctuate drastically. Supporting Information Video SI shows that once these light spots stopped moving, i.e., the water evaporated completely and all particles aggregated and were deposited onto the solid surface, the large SERS enhancement was quenched. According to theoretical simulations, a large enhancement of the electric field occurs only when the interparticle gap is less than 3 nm. As the gap decreases from 3 to 0 nm, the droplet height decreases only from 3 to 2.5 μm (Supporting Information Figure S6f). The focal depth was approximately 9.6 μm in our configuration, and the effect of the focal depth therefore was clearly weak. As all of the particles moved toward the laser center in the final stage of evaporation, the number of particles increased by only approximately 12% within the scope of the focal spot. However, the SERS signal intensity increased by 3 orders of magnitude. Thus, the sharp decrease in SERS intensity was not caused by the location of the laser focus, as further demonstrated by the well-focused line mapping in the dry state. These results strongly support our theoretical model of the 3D hotspot matrix.

After the time-course SERS mapping described above, line mapping was performed to evaluate the differences at various sampling positions (Supporting Information Video SII). The quality of the line-mapping spectra is somewhat poor, although

the R6G features can be distinguished at all 201 positions (Figure 6e). However, all intensities of the 610 cm^{-1} peak are less than 425 cps, and the average intensities is 230 ± 44 cps (Figure 6f). Thus, our technique produced an additional SERS enhancement of 2 orders of magnitude compared to the dried substrates. In particular, the SERS intensities near the zero position (the position used for the time-course mapping) were slightly lower than those at other positions. Many additional effects may arise after the laser irradiation of the sample under dry conditions:[37] photobleaching, photodesorption, photoinduced surface diffusion, substrate heating, or possibly changes in the substrate morphology (through photo-oxidation, for example), all of which could easily cause SERS signal to deteriorate. The presence of water may protect the analytes from photochemistry or photobleaching induced directly by the laser and contribute to stabilizing the peak frequency and narrowing the peak fwhm.

When the amount of R6G in the system was reduced to 5 amol, it became very difficult to acquire a spectrum with a tolerable signal-to-noise ratio for a dried sample (Supporting Information Figure S10b, histograms). By contrast, significant SERS signals were predicted for even 0.5 amol of R6G molecules in the 3D hotspot matrix, and such signals could be feasibly recorded (Supporting Information Figure S10a,b, solid circles). Considering an area ratio of approximately 3×10^5 ($\pi \times 0.4^2$ mm^2/$\pi \times 0.65^2$ μm^2) between the deposition area and the laser spot and assuming uniform distributions of all particles and molecules, there was an average of one R6G molecule (0.5 amol $\times 6 \times 10^{23}$ molecules·mol^{-1}/3×10^5) within the scope of the laser spot. In other words, a single molecule of R6G residing in the 3D hotspot matrix can exhibit efficient Raman enhancement. Ten repeated experiments were conducted. The standard deviation of the maximum SERS intensities for 50 amol of R6G was less than 15%, but that for 0.5 amol of R6G was more than 58% (Supporting Information Figure S10c), which may have been caused by the increased uncertainty in the number of molecules present in the 3D hotspot matrix. Nevertheless, each measurement acquired clear and distinguishable SERS signals of R6G at the single-molecule level. With regard to the tremendous electric-field gradient in the 3D hotspot matrix, optical trapping of the molecules,[38] analogous to the optically biased diffusion of R6G in solution, is suspected (Supporting Information Section S3.7).[39] These aspects of optical forces have only begun to be explored and have only been reported in a small number of situations to date;[37] our technique might offer an excellent method of utilizing the optical-trapping effect in SERS measurements, even though the true situation may be much more complicated.

The sensitivity and limit of detection (LOD) for this platform were evaluated by varying the amounts of R6G molecules from 0.05 amol to 0.5 nmol in 1-μL Ag sols (Supporting Information Figure S10c,d). Because 500 fmol of R6G could induce saturation of the CCD detector under 100% laser power, the measurements were performed under two different sets of measurement conditions: those for R6G amounts of 0.05−50 amol were performed using 100% laser power, whereas those for R6G amounts of 50 amol to 0.5 nmol were performed using 10% laser power. The maximum intensities of the characteristic R6G band at 610 cm^{-1} measured in the experiments that used 100% laser power and 10% laser power are plotted as functions of the R6G concentration in Supporting Information Figure S10c,d, respectively. The experimental data were obtained from at

least three independent experiments for each concentration. It is interesting to note that the maximum intensities varied slightly when the R6G amounts were below 5 amol. Moreover, these data in the range of 0.05 to 50 amol were well fitted by a Langmuir isotherm curve using nonlinear least-squares regression (Supporting Information Figure S10c). By substituting three standard deviations of the blank signal into the fitted Langmuir isotherm curve, an estimated LOD of at least 0.05 amol was obtained. The Langmuir-isotherm fitting might indicate submonolayer or monolayer adsorption of R6G on the Ag particles and may further suggest that there is a limit on the number of R6G molecules that can be accommodated by the 3D hotspot matrix. When many more molecules are present in the system, the signal should become more sensitive to the R6G concentration and should follow a linear relation with the concentration. This speculation is consistent with the experimental data obtained for amounts of R6G in the range of 50 amol to 0.5 nmol (Supporting Information Figure S10d). The linear data fitting is in good agreement with the theoretical analysis to a certain instructional significance, even though the true situation may be more complicated than the theoretical model. The nonlinear results are also consistent with previous reports.[40,41] The experiments concerning sensitivity and LOD demonstrated the excellent performance of the 3D hotspot matrix compared with that of dried substrates and also implied that the 3D hotspot matrix suppressed many additional effects that could obscure weak signals from the target analytes. Another advantage of our platform is that only small amounts of sample are necessary; no further concentration or enrichment is required.

As an effort directed toward a universal SERS platform, we also examined two nonresonant molecules under similar conditions. The first molecule was *p*-aminothiophenol (PATP), which is a widely used SERS reporter and adsorbs on Ag as thiolate after S−H bond cleavage.[42] The Raman fingerprint peaks of 50 fmol of PATP cannot be distinguished under dried conditions; nevertheless, they were clearly exhibited in the evaporation process, and even 50 amol of PATP was able to generate identifiable characteristics in the SERS signal[42] (Figure 7a). The second molecule tested was diethyl 4-nitrophenyl phosphate (Paraoxon, Figure 7b), which is a liposoluble pesticide with much weaker binding on Ag surfaces. Our results demonstrate that it becomes quite difficult to acquire the Raman fingerprint peaks of 0.1 nmol of Paraoxon molecules under dried conditions (data not shown). Nevertheless, signals from even 0.1 fmol of Paraoxon could be reliably recorded using our technique. The 3D hotspot matrix increases the SERS sensitivity by at least 3 orders of magnitude for both PATP and Paraoxon molecules, demonstrating that hotspots in 3D space are quite powerful and more effective than those in a dried substrate.

Because of the robust and ultrahigh Raman enhancement and the molecule-trapping capability of the 3D hotspot matrix, a portable Raman spectrometer could be used to successfully detect a variety of ultratrace analytes that contained different functional groups, such as the pyridine ring on 4-mercaptopyridine (MPY, Figure 8a), the nitro group on nitrobenzene (NP, Figure 8b), the primary amine group on methylamphetamine (MAMP, Figure 8c), and the secondary amine group on 3,4-methylenedioxymethamphetamine hydrochloride (MDMA-HCl, Figure 8d). The presence of a thiol, amine, phosphate, or nitro moiety on the molecules leads to different binding efficiencies with the metal surface and thus yields different
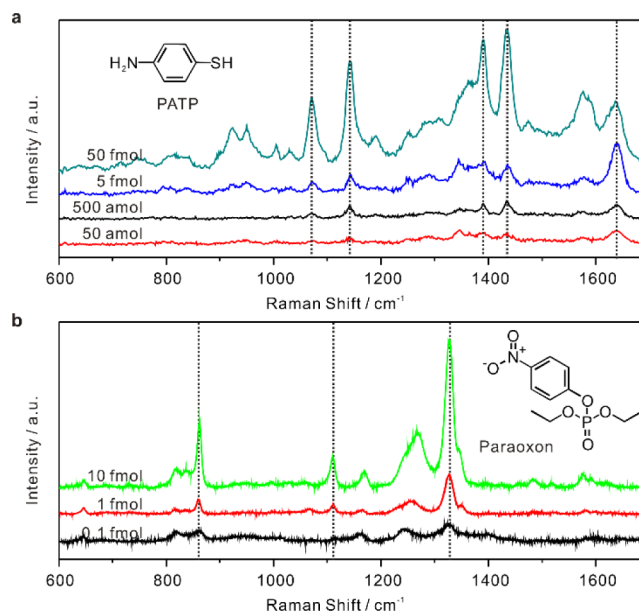

Figure 7. 3D hotspots for the detection of analytes of different affinities for a citrate-capped metal surface.
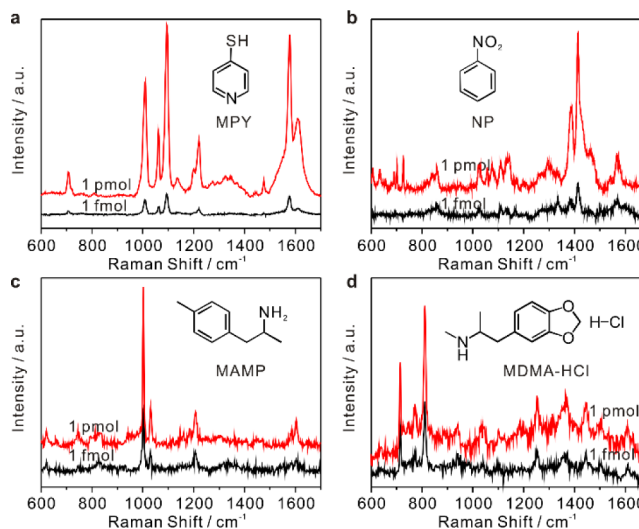

Figure 8. 3D hotspots for the detection of analytes with different functional groups using a portable Raman spectrometer.

Raman enhancements. Nevertheless, for all these analytes, the SERS signals could be easily recorded, even at the level of 1 fmol, using a portable Raman spectrometer, and the signal-to-noise ratio and sensitivity were much better than those obtained using dried substrates, especially for two types of drugs: MAMP and MDMA-HCl. A final observation is that gold nanoparticle sols exhibit characteristics similar to all those discussed above.[43] Our technique may offer the only viable methodology proposed to date for accessing and manipulating a molecule into hotspots in 3D space by exploiting the synergistic interactions among the adhesive force, electrostatic repulsion, van der Waals attraction, and the optical-trapping effect. This method offers powerful detection capabilities with respect to trapping and detecting analytes with either weak binding or low Raman cross sections, and furthermore, it can be applied via an easily used and field-portable analyzer.

CONCLUSIONS

A 3D hotspot matrix was experimentally and theoretically demonstrated; it was simply achieved by evaporating a droplet of citrate-Ag sols on a fluorosilylated silicon wafer. On the basis of the comprehensive experimental data and theoretical simulations, it was found that the evaporation process produces a distinct 3D geometry with minimal polydispersity of particle size and maximal uniformity of interparticle distance, both of which are significantly different from the dry state, and this 3D geometry can certainly host a large number of hot spots in 3D space and amplify the SERS enhancement accordingly. The universality of the platform reported here can extend the use of 3D hotspots to other fields by permitting the incorporation of either different materials, such as spherical core–shell nanoparticles and nanoshells, or different spectroscopic methods, such as surface-enhanced fluorescence, UV, or IR. The concept of 3D hotspots can allow easy access to and manipulation of a molecule in 3D space by the exploitation of the optical-trapping effect and promises a wide variety of potential applications in in situ observations of plasmon-enhanced chemical reactions. These 3D hotspots can enable electromagnetic characteristics that are not yet achievable in currently extant nanostructures as well as novel approaches to current technological challenges, such as high-throughput chemical and biological sensing.

ASSOCIATED CONTENT

ⓈSupporting Information

Synthesis and characterizations of the Ag sols; preparation of the extremely dilute solutions; SERS experiments and data processing; adsorbing behaviors of citrate-Ag sols on hydrophobic-treated silicon wafer; liquid-bridged Ag particles and the estimation of the adhesive force; the particle–particle interaction energy profiles; estimation of the colloidal stability in the late-stage evaporation process; 3D Monte Carlo method simulation of the number of hotspots; finite element method simulation of the electric field distributions; optical trapping effects of 3D hotspot matrix; 3D hotspot matrix for detecting single-molecules of R6G; supplementary videos. This material is available free of charge via the Internet at http://pubs.acs.org.

AUTHOR INFORMATION

Corresponding Author

lbyang@iim.ac.cn; jhliu@iim.ac.cn

Notes

The authors declare no competing financial interest.

ACKNOWLEDGMENTS

REFERENCES

(1) Willets, K. A.; Van Duyne, R. P. *Annu. Rev. Phys. Chem.* **2007**, *58*, 267.

(2) Xu, H. X.; Bjerneld, E. J.; Kall, M.; Borjesson, L. *Phys. Rev. Lett.* **1999**, *83*, 4357.

(3) Anker, J. N.; Hall, W. P.; Lyandres, O.; Shah, N. C.; Zhao, J.; Van Duyne, R. P. *Nat. Mater.* **2008**, *7*, 442.

(4) Luk'yanchuk, B.; Zheludev, N. I.; Maier, S. A.; Halas, N. J.; Nordlander, P.; Giessen, H.; Chong, C. T. *Nat. Mater.* **2010**, *9*, 707.

(5) Li, J. F.; Huang, Y. F.; Ding, Y.; Yang, Z. L.; Li, S. B.; Zhou, X. S.; Fan, F. R.; Zhang, W.; Zhou, Z. Y.; WuDe, Y.; Ren, B.; Wang, Z. L.; Tian, Z. Q. *Nature* **2010**, *464*, 392.

(6) Nam, J. M.; Lim, D. K.; Jeon, K. S.; Hwang, J. H.; Kim, H.; Kwon, S.; Suh, Y. D. *Nat. Nanotechnol.* **2011**, *6*, 452.

(7) Talley, C. E.; Jackson, J. B.; Oubre, C.; Grady, N. K.; Hollars, C. W.; Lane, S. M.; Huser, T. R.; Nordlander, P.; Halas, N. J. *Nano Lett.* **2005**, *5*, 1569.

(8) Nam, J. M.; Lim, D. K.; Jeon, K. S.; Kim, H. M.; Suh, Y. D. *Nat. Mater.* **2010**, *9*, 60.

(9) Chen, G.; Wang, Y.; Yang, M. X.; Xu, J.; Goh, S. J.; Pan, M.; Chen, H. Y. *J. Am. Chem. Soc.* **2010**, *132*, 3644.

(10) Lee, A.; Andrade, G. F. S.; Ahmed, A.; Souza, M. L.; Coombs, N.; Tumarkin, E.; Liu, K.; Gordon, R.; Brolo, A. G.; Kurnacheva, E. *J. Am. Chem. Soc.* **2011**, *133*, 7563.

(11) Wang, H.; Levin, C. S.; Halas, N. J. *J. Am. Chem. Soc.* **2005**, *127*, 14992.

(12) Dickson, W.; Wurtz, G. A.; Evans, P. R.; Pollard, R. J.; Zayats, A. V. *Nano Lett.* **2008**, *8*, 281.

(13) Chen, H. L.; Hsieh, K. C.; Lin, C. H.; Chen, S. H. *Nanotechnology* **2008**, *19*, 435304.

(14) Xu, G.; Huang, C. M.; Tazawa, M.; Jin, P.; Chen, D. M. *J. Appl. Phys.* **2008**, *104*, 053102.

(15) Alexander, K. D.; Skinner, K.; Zhang, S.; Wei, H.; Lopez, R. *Nano Lett.* **2010**, *10*, 4488.

(16) Liu, H.; Sun, Y.; Jin, Z.; Yang, L.; Liu, J. *Chem. Sci.* **2013**, *4*, 3490.

(17) Xu, H. X.; Aizpurua, J.; Kall, M.; Apell, P. *Phys. Rev. E: Stat. Phys., Plasmas, Fluids, Relat. Interdiscip. Top.* **2000**, *62*, 4318.

(18) Haynes, C. L.; Van Duyne, R. P. *J. Phys. Chem. B* **2001**, *105*, 5599.

(19) Konishi, T.; Kiguchi, M.; Takase, M.; Nagasawa, F.; Nabika, H.; Ikeda, K.; Uosaki, K.; Ueno, K.; Misawa, H.; Murakoshi, K. *J. Am. Chem. Soc.* **2013**, *135*, 1009.

(20) Theiss, J.; Pavaskar, P.; Echternach, P. M.; Muller, R. E.; Cronin, S. B. *Nano Lett.* **2010**, *10*, 2749.

(21) Negishi, R.; Hasegawa, T.; Terabe, K.; Aono, M.; Ebihara, T.; Tanaka, H.; Ogawa, T. *Appl. Phys. Lett.* **2006**, *88*, 223111.

(22) Cecchini, M. P.; Turek, V. A.; Paget, J.; Kornyshev, A. A.; Edel, J. B. *Nat. Mater.* **2013**, *12*, 165.

(23) Kim, K.; Han, H. S.; Choi, I.; Lee, C.; Hong, S.; Suh, S.-H.; Lee, L. P.; Kang, T. *Nat. Commun.* **2013**, *4*, 2182.

(24) Urban, A. S.; Shen, X.; Wang, Y.; Large, N.; Wang, H.; Knight, M. W.; Nordlander, P.; Chen, H.; Halas, N. J. *Nano Lett.* **2013**, *13*, 4399.

(25) Polte, J.; Ahner, T. T.; Delissen, F.; Sokolov, S.; Emmerling, F.; Thunemann, A. F.; Kraehnert, R. *J. Am. Chem. Soc.* **2010**, *132*, 1296.

(26) Ilavsky, J.; Jemian, P. R. *J. Appl. Crystallogr.* **2009**, *42*, 347.

(27) Shi, L.; Jing, C.; Ma, W.; Li, D.-W.; Halls, J. E.; Marken, F.; Long, Y.-T. *Angew. Chem.* **2013**, *125*, 6127.

(28) Yunker, P. J.; Still, T.; Lohr, M. A.; Yodh, A. G. *Nature* **2011**, *476*, 308.

(29) Lyonnard, S.; Bartlett, J. R.; Sizgek, E.; Finnie, K. S.; Zemb, T.; Woolfrey, J. L. *Langmuir* **2002**, *18*, 10386.

(30) Ghosh, S. K.; Pal, T. *Chem. Rev.* **2007**, *107*, 4797.

(31) Petosa, A. R.; Jaisi, D. P.; Quevedo, I. R.; Elimelech, M.; Tufenkji, N. *Environ. Sci. Technol.* **2010**, *44*, 6532.

(32) Gregory, J. *J. Colloid Interface Sci.* **1981**, *83*, 138.

(33) Gregory, J. *J. Colloid Interface Sci.* **1975**, *51*, 44.

(34) El Badawy, A. M.; Aly Hassan, A.; Scheckel, K. G.; Suidan, M. T.; Tolaymat, T. M. *Environ. Sci. Technol.* **2013**, *47*, 4039.

(35) Mcdowellboyer, L. M. *Environ. Sci. Technol.* **1992**, *26*, 586.

(36) Israelachvili, J. N. *Intermolecular and Surface Forces*; 3rd ed.; Academic Press, Elsevier: London, 2011.

(37) Le Ru, E. C.; Etchegoin, P. G. *Principles of Surface-Enhanced Raman Spectroscopy*; Elsevier: Oxford, 2009.

(38) Xu, H. X.; Kall, M. *Phys. Rev. Lett.* **2002**, *89*, 246802.

(39) Osborne, M. A.; Balasubramanian, S.; Furey, W. S.; Klenerman, D. *J. Phys. Chem. B* **1998**, *102*, 3160.

(40) Lu, L.-Q.; Zheng, Y.; Qu, W.-G.; Xu, A.-W.; Yu, H.-Q. *J. Mater. Chem.* **2012**, *22*, 20986.

(41) Guo, Y. B.; Oo, M. K. K.; Reddy, K.; Fan, X. D. *ACS Nano* **2012**, *6*, 381.

(42) Choi, H.-K.; Shon, H. K.; Yu, H.; Lee, T. G.; Kim, Z. H. *J. Phys. Chem. Lett.* **2013**, *4*, 1079.

(43) For simplicity, the part on Au sols for constructing 3D hotspot matrix will be published in the future.

5341

dx.doi.org/10.1021/ja501951v | *J. Am. Chem. Soc.* 2014, 136, 5332−5341